PNAS RESEARCH ARTICLE | BIOPHYSICS AND COMPUTATIONAL BIOLOGY

Intrinsically disordered region amplifies membrane remodeling to augment selective ER-phagy

Sergio Alejandro Poveda-Cuevas[a,b], Kateryna Lohachova[a,b], Borna Markusic[a,c], Ivan Dikic[a,b], Gerhard Hummer[d,e], and Ramachandra M. Bhaskara[a,b,1]

Affiliations are included on p. 11.

Edited by Ken Dill, Stony Brook University, Stony Brook, NY; received April 22, 2024; accepted August 27, 2024

Intrinsically disordered regions (IDRs) play a pivotal role in organellar remodeling. They transduce signals across membranes, scaffold signaling complexes, and mediate vesicular traffic. Their functions are regulated by constraining conformational ensembles through specific intra- and intermolecular interactions, physical tethering, and posttranslational modifications. The endoplasmic reticulum (ER)-phagy receptor FAM134B/RETREG1, known for its reticulon homology domain (RHD), includes a substantial C-terminal IDR housing the LC3 interacting motif. Beyond engaging the autophagic machinery, the function of the FAM134B-IDR is unclear. Here, we investigate the characteristics of the FAM134B-IDR by extensive modeling and molecular dynamics simulations. We present detailed structural models for the IDR, mapping its conformational landscape in solution and membrane-anchored configurations. Our analysis reveals that depending on the membrane anchor, the IDRs collapse onto the membrane and induce positive membrane curvature to varying degrees. The charge patterns underlying this Janus-like behavior are conserved across other ER-phagy receptors. We found that IDRs alone are sufficient to sense curvature. When combined with RHDs, they intensify membrane remodeling and drive efficient protein clustering, leading to faster budding, thereby amplifying RHD remodeling functions. Our simulations provide a perspective on IDRs of FAM134B, their Janus-like membrane interactions, and the resulting modulatory functions during large-scale ER remodeling.

IDRs | structural ensemble | conformational entropy | curvature induction | ER remodeling

Significance

The extent of intrinsic disorder in membrane remodeling remains unclear. Here, we focus on the C-terminal disordered region of FAM134B, a protein involved in the endoplasmic reticulum (ER) recycling process. Through advanced computer modeling and extensive simulations, we show how membrane-anchored disordered protein segments exhibit different ensemble properties. This context-dependent behavior is sequence-encoded and shared among other proteins involved in ER-phagy. Membrane anchoring alone enables disordered regions to sense and influence local membrane shape, and when combined with other membrane-shaping elements, they accelerate large-scale membrane remodeling. These insights deepen our understanding of disordered segments and how they influence membrane shapes.

Exploring the human proteome reveals a complex and dynamic landscape woven into an intricate protein network that governs a diverse array of cellular processes. A significant subset contains intrinsically disordered regions (IDRs), segments that lack a stable 3D structure under physiological conditions (1). The diversity of IDRs within the human proteome plays a pivotal role in regulating a vast array of cellular functions (2). From facilitating protein-protein interactions (PPIs) and signal transduction to orchestrating transcriptional and posttranslational modifications (PTMs), IDRs serve as versatile modules contributing to the complexity and adaptability of the cellular machinery (1). Further, multivalent interactions of the IDRs promote liquid-liquid phase separation (LLPS) to form condensates, which concentrate specific proteins and nucleic acids for localized cellular action (3).

Membrane-associated and membrane-anchored IDRs have emerged as dynamic mediators of processes occurring at the surface of membrane-bound organelles (2). IDRs adopt diverse biochemical and biophysical principles to actively bind and modulate membrane functions, e.g., by folding of disordered regions upon membrane binding (disorder-to-order transitions) and by forming amphipathic helices (AHs) that induce or sense membrane curvature (2). 2D confinement of IDRs to membranes increases their effective concentration and limits the search space for IDR-mediated PPIs, thereby enhancing protein association and crowding (4, 5). The length and amino acid pattern of the IDRs control the sampled space around the membrane and the ability to engage with binding partners ("fly-casting") (6). PTMs on the IDRs regulate membrane-binding (7) and modulate signaling cascades (8). Multivalent low-affinity interactions of membrane-bound IDRs could also drive clustering and phase separation (LLPS) at the membrane (9). These distinct mechanisms or their blends play a pivotal role in organellar remodeling (2).

Selective endoplasmic reticulum (ER)-phagy, a critical homeostatic pathway, orchestrates the targeted degradation of the ER via autophagy, particularly under stress or ER expansion (10). ER-phagy is emerging as a crucial catabolic pathway that i) rapidly mobilizes nutrients during starvation (10), ii) actively regulates the size

Author contributions: G.H. and R.M.B. designed research; S.A.P.-C., K.L., B.M., and R.M.B. performed research; I.D., G.H., and R.M.B. contributed new reagents/analytic tools; S.A.P.-C., K.L., B.M., I.D., G.H., and R.M.B. analyzed data; and S.A.P.-C. and R.M.B. wrote the paper.

The authors declare no competing interest.

This article is a PNAS Direct Submission.

[1]To whom correspondence may be addressed. Email: Bhaskara@med.uni-frankfurt.de.

This article contains supporting information online at https://www.pnas.org/lookup/suppl/doi:10.1073/pnas.2408071121/-/DCSupplemental.

Published October 25, 2024.

and shape of the ER (11), iii) ensures clearance of aberrant or aged proteins and lipids (12), iv) is co-opted by pathogens to invade host cells (13), and v) is deregulated in an increasing number of diseases (14). Integral to this process is the recruitment of the phagophore membrane to the ER-phagy sites by distinct membrane-bound receptors (15). FAM134B/RETR1, and all known ER-phagy receptors, including SEC62, RTN3, CCPG1, and TEX264, are ER-resident integral membrane proteins that house LC3 interacting regions (LIRs) in their cytoplasmic IDRs (10). The IDRs serve as flexible and extensible connections between their ER anchor and the LC3/ATG8 proteins covalently attached to the phagophore membrane, which results in the recruitment of the autophagic machinery to the ER.

Selective ER-phagy closely intertwines with ER membrane remodeling. As autophagic membranes are engaged, the ER membrane undergoes large-scale shape changes, leading to fragmentation and engulfment into the autophagosomes (15). Recent advances combining cell biology methods, in vitro membrane remodeling assays, and extensive molecular dynamics (MD) simulations have identified and mapped the curvature induction, sensing, and sorting functions of the ER-phagy receptors. For instance, FAM134B, RTN3, and TEX264 have membrane-sculpting transmembrane (TM) hairpins and AHs (10). The transmembrane domains of these receptors, particularly the RHDs, adopt a dynamic wedge shaped membrane inclusion, sculpting the ER-membrane (17). Additionally, their curvature sensing functions trigger protein sorting and clustering to nucleate membrane buds spontaneously (18). This process is further fine-tuned and accelerated by the ubiquitination of receptors (19) to form large membrane-associated homomeric and heteromeric RHD clusters (20) to enhance ER-phagy. However, the precise functions and role of IDRs within ER-phagy receptors in these various steps remain unclear. The importance of IDRs, especially in the context of membrane remodeling, has not been addressed.

Studying remodeling properties of membrane-associated and membrane-anchored IDRs presents several challenges. The IDR conformations can be variable in solution and membrane-bound states due to differential interactions with solvent and distinct lipid species (1, 2, 21). The large conformational entropy of the membrane-bound IDRs is favored by underlying bent and curved bilayer geometry, as demonstrated experimentally for AP180, amphiphysin, and epsin (22, 23). The increased surface density of IDRs can also perturb bilayers (4). IDRs crowded on one side of the membrane surfaces can induce substantial lateral pressure in one of the leaflets (24, 25), resulting in dramatic curvature induction. The interplay between the electrostatic and entropic effects, the presence of other membrane-shaping elements (e.g., TM hairpins or AHs), and the crowding effects of tethered IDRs are often challenging to decouple in experiments (25). With unmapped relative contributions, the importance of IDRs is often undermined in membrane remodeling.

Here, we aim to decouple the diverse roles of the IDRs in ER-phagy receptors. We use extensive modeling and simulations of the IDR of FAM134B, a well-studied ER-phagy receptor model system, to investigate how the IDR structure and dynamics influence local membrane properties. To this end, we build detailed structural ensembles of the IDR. We use MD simulations to explore its conformational landscape in solution and varied membrane-anchored states. We identify that the FAM134B-IDR adopts alternate conformational states based on the membrane anchor. Our simulations reveal that the IDR alone can induce and sense membrane curvature. This effect accentuates the RHD-mediated curvature induction and curvature sensing functions to promote efficient clustering, nucleating membrane buds faster, thereby boosting selective ER-phagy. Our findings suggest that the C-terminal IDR modulates the membrane-shaping functions of the RHD along the various phases of ER-phagy.

Results

Structure of FAM134B-IDR. The well-characterized RHD of FAM134B (17) is flanked by two intrinsically disordered fragments on the cytosolic side of the ER membrane, i.e., a smaller N-terminal IDR (1 to 79) and a longer C-terminal IDR (261 to 497) that houses the functional LIR motif (^{453}DDFELL^{458}; Fig. 1*A*). Analysis of the residue composition of these segments

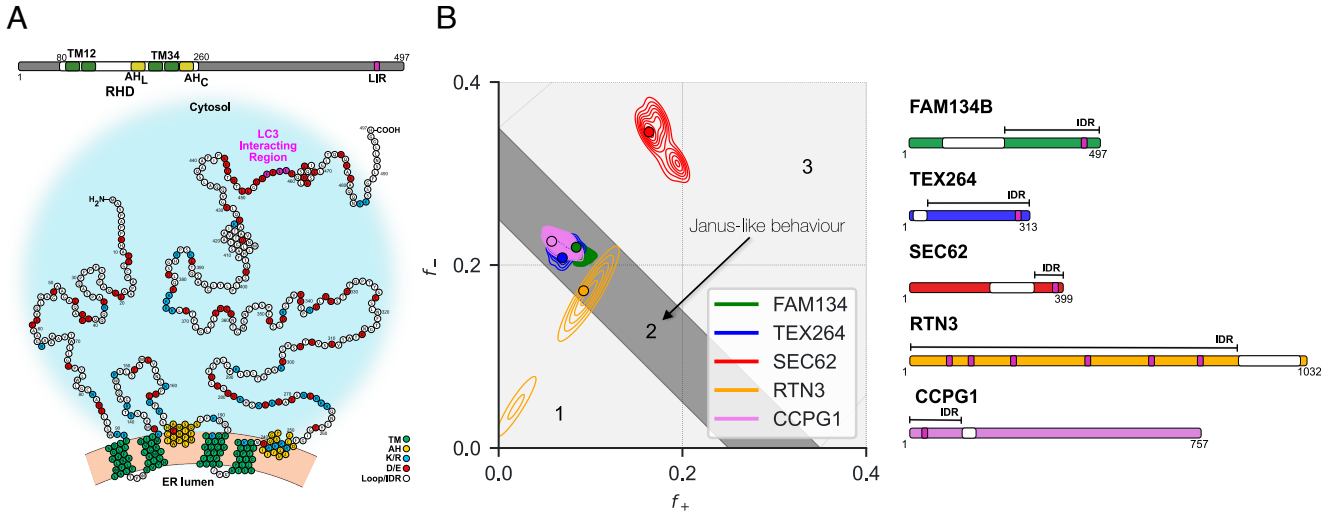

Fig. 1. IDRs of selective ER-phagy receptors. (*A*) Domain structure (*Top*) and topology (*Bottom*) of full-length FAM134B. The topology diagram shows the organization of the membrane-bound RHD (green and yellow; 80 to 260) in the curved bilayer (orange). The RHD is flanked by the N-terminal (1 to 79) and C-terminal (261 to 497) disordered regions on the cytosolic side of the bilayer. Charged residues (blue or red) and the functional LC3 interacting region (purple) within the IDRs are highlighted. (*B*) Das-Pappu diagram (16) (*Left*) plotting the fraction of positive (f_+; K and R) against the fraction of negative (f_-; D and E) residues for ER-phagy receptors (*Right*). Colored contours show the probability densities estimated from 500 homologous IDR segments corresponding to each known human ER-phagy receptor (filled circles). Regions 1 and 3 of the phase diagram correspond to IDRs with polar tracts (globular or tadpole-like structures) and polyampholytes (coils, hairpins, and chimeric structures), respectively. Region 2 (dark gray) is the transition zone, representing Janus-like quality adopting collapsed or expanded IDR structures.

revealed several contiguous stretches of 3 to 5 charged residues (red or blue regions; Fig. 1*A*). We compared the charge characteristics of the C-terminal disordered fragment (referred to hereafter as IDR) of the FAM134 family along with the cytosolic IDRs of other ER-phagy receptor families (*SI Appendix*, Fig. S1 and Table S1). By quantifying the distribution of fractional positive and negative charges within the IDR, we grouped the ER-phagy receptors based on the Das-Pappu classification (16) for IDRs (Fig. 1*B*). We found that they predominantly correspond to the boundary region (Region 2) between weak and strong polyampholytes, indicative of adopting chimeric structures between more globule-like and partially open tadpole or coil structures (Fig. 1*B*). Only the SEC62-IDRs correspond to Region 3, indicating more coil-like structures of a strong polyampholyte.

We analyzed the FAM134B sequence to examine the predicted features of the IDR (*SI Appendix*, Fig. S2*A*). An analysis of the AlphaFold2 (AF) model (*SI Appendix*, Fig. S2 *B* and *C*) of the IDR revealed a predominantly coil-like structure with three distinct high-confidence regions with more local contacts (pLDDT $\geq$ 80; R1, R2, and R3 in *SI Appendix*, Fig. S2*B*), indicating a partial local residual helical structure for the IDR. Furthermore, these regions also correspond to the predicted PPI sites of FAM134B (Molecular Recognition Features in *SI Appendix*, Fig. S2*A*), which indicates possible functional constraints to preserving the local helical structure.

Next, we obtained a structural ensemble for the IDR of FAM134B in solution by running 1 μs of atomistic MD simulation starting from the AF model (Fig. 2*A* and *SI Appendix*, Table S2). We found that the IDR ensemble populated relatively compact structures in solution (Fig. 2*A*) with end-to-end distances of $R_e \approx 4 \pm 2$ nm and radii of gyration of $R_g \approx 2.6 \pm 0.5$ nm (mean ± SD). The corresponding 2D free energy surface is shown in Fig. 2*B*. The local secondary structure remained predominantly coil-like (Fig. 2*C*; see P_C; blue curve). However, the three residual helical stretches (R1, R2, and R3) remained relatively stable (up to 1 μs), with only the N-terminal R1-helix undergoing partial unfolding (Fig. 2*C*; see P_H; green curve). We detected that distinct pairwise residue interactions (apolar: S366-L373, L458-L463, and salt bridge: K376-D381) contribute to the stability of the compact structure of the IDR in solution (*SI Appendix*, Fig. S2*D*).

Subsequently, we constructed an effective coarse-grained (CG) model of the IDR to study its motions and its coupling to the RHD. We used the Martini model with reduced protein–protein interaction strength (Fig. 2 *D–F* and *SI Appendix*, Table S2; see *Methods*) to model the IDR. We used alpha-scaling (26, 27) to vary the PPI strength in a range between $\alpha = 1.0$ (full interaction) to $\alpha = 0.3$ (30% interaction). In this way, we gradually reduced the stickiness of the Martini model, increasingly sampling less compact and more open conformations of the IDR (*SI Appendix*, Fig. S3 *A–D*). At $\alpha = 0.6$, we found the free energy surface of the IDR extracted from the scaled coarse-grained MD simulations to be consistent with that obtained from atomistic MD simulations (Fig. 2 *B* and *E* and *SI Appendix*, Fig. S3*C*). Moreover, at $\alpha = 0.6$, we also found that the values of R_g and R_e averaged over the ensemble also matched closely (*SI Appendix*, Fig. S3 *C, E,* and *F*). For RNA-binding protein FUsed in Sarcoma (FUS), similar α values gave phase behavior consistent with experiments (27). The good overlap of the free-energy surfaces of the all-atom and coarse-grained IDR ensembles encouraged us to use $\alpha = 0.6$ to model the effective interactions of the IDR in all subsequent MD simulations.

FAM134B-IDR Collapses onto the RHD. To determine whether the tethering of the IDR at its N terminus influences its ensemble properties, we modeled two membrane-anchored IDRs. The N terminus of the IDR was linked to either $KALP_{25}$, a model

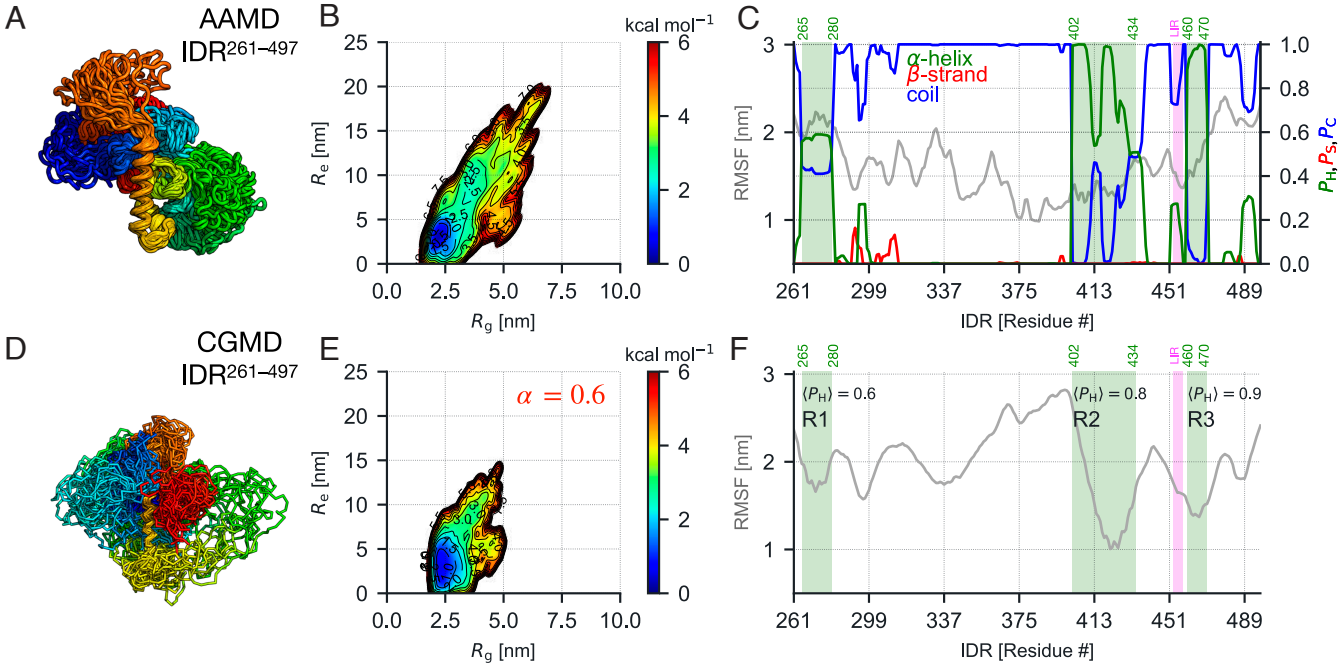

Fig. 2. Structural models for FAM134B-IDR in solution. (*A*) IDR ensemble (30 representative structures; rainbow colors) in a dilute solution sampled in atomistic MD simulations. (*B*) Free energy landscape for the IDR ensemble along the radius of gyration (R_g) and end-to-end distances (R_e) from atomistic MD simulations. (*C*) Root mean square fluctuations (RMSF; gray curve) and secondary structure propensities (helix: green, strand: red, and coil: blue) along the IDR length were obtained from all-atom simulations to quantify the local conformational variability. (*D*) Representative IDR structures from coarse-grained MD simulations obtained after scaling protein–protein interaction strength ($\alpha = 0.6$) to calibrate the (*E*) coarse-grained free energy landscape. (*F*) Regions R1, R2, and R3 (green-shaded) display high local helix propensity ($\langle P_H \rangle \geq 0.5$) and reduced fluctuations in coarse-grained simulations.

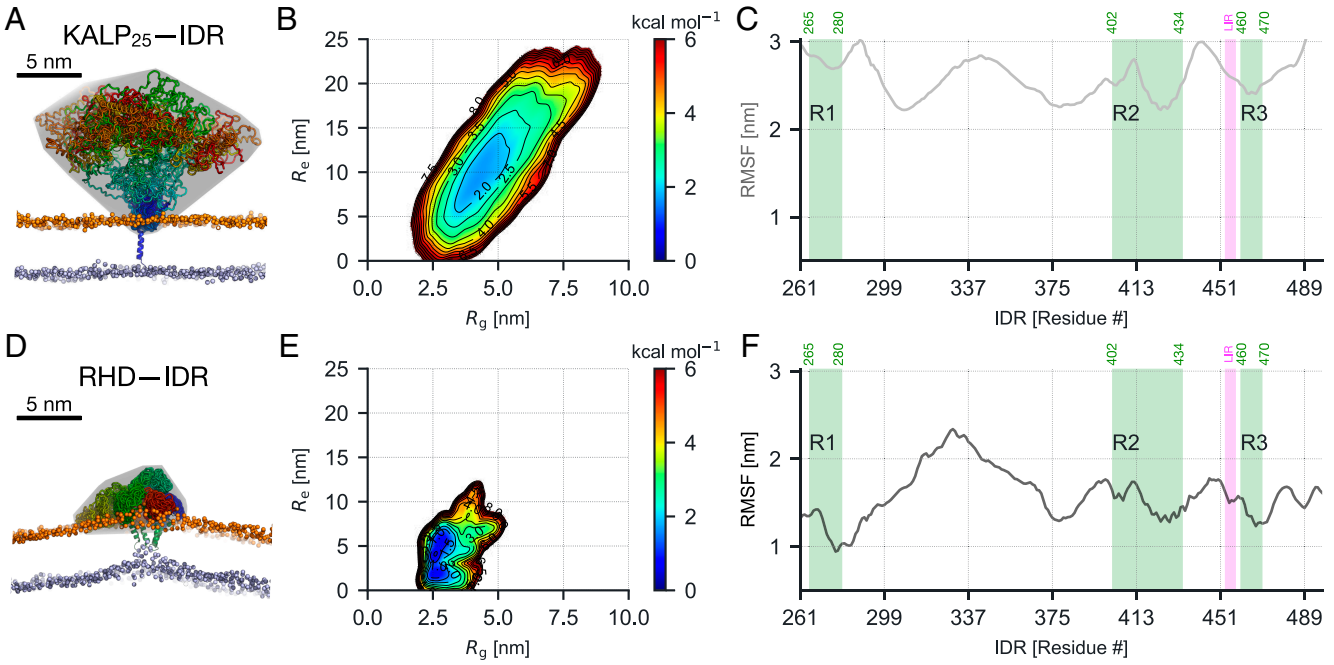

Fig. 3. Membrane anchoring influences the conformation of IDRs in coarse-grained MD simulations. Ensemble properties of membrane-anchored IDRs were obtained by connecting them in tandem to the C terminus of (*A*–*C*) the $KALP_{25}$ peptide ($KALP_{25}$–IDR) or (*D*–*F*) the FAM134B-RHD structure (RHD–IDR). (*A* and *D*) 30 representative conformations (rainbow-colored) of each IDR ensemble aligned to the membrane-bound KALP peptide or RHD. Gray envelope shows their corresponding hydrodynamic volumes (*SI Appendix*, Fig. S4) on the cytosolic side. (*B* and *E*) Free energy surfaces of IDRs linked to $KALP_{25}$ and RHD along R_g and R_e. (*C* and *F*) $KALP_{25}$–IDR displays larger fluctuations, sampling a larger conformational space. By contrast, the RHD induces compaction of the tethered IDR, inducing the formation of a membrane scaffold stabilized by specific intramolecular and bilayer interactions of the IDR (*SI Appendix*, Fig. S6).

transmembrane helical peptide ($KALP_{25}$–IDR), or to the RHD of FAM134B (80 to 497; RHD–IDR). We then embedded these two constructs in flat model bilayers containing 1-palmitoyl-2-oleoyl-sn-glycero-3-phosphocholine (POPC) lipids and initiated MD simulations (*SI Appendix*, Table S3). The IDR anchored to the $KALP_{25}$ peptide adopted more extended structures (Fig. 3*A*) with a larger conformational landscape (Fig. 3*B*), and high flexibility (Fig. 3*C*). Further, this IDR ensemble displayed high asphericity ($\approx 0.4 \pm 0.2$; *SI Appendix*, Fig. S4*A*), enclosed a much larger hydrodynamic volume above the membrane (gray envelopes in Fig. 3 *A* and *D* and corresponding radii, $R_T \approx 4.5 \pm 2.0$ nm; *SI Appendix*, Fig. S4 *B* and *C*) as opposed to compact conformations of the IDR in solution. By contrast, the IDR tethered to the membrane-bound RHD collapsed quickly (within the first 300 ns) and adopted more compact structures on top of the RHD (Fig. 3*D* and *SI Appendix*, Fig. S4 *A*–*C*) akin to IDRs in solution. We found that the extent of collapse and compaction of the RHD-anchored IDR, albeit smaller than the solution-phase IDR, was consistent in three different replicates, indicating that more specific interactions stabilized this intermediate structure.

An analysis of the contact maps of the IDR ensembles averaged from MD simulations (*SI Appendix*, Fig. S5 *A*–*C*) revealed that the overall character was preserved. Still, the intensities of specific residue-wise contacts varied under the different contexts of the IDR studied (unbound and anchored). We found that the compaction of the IDR in solution and partially in the RHD-anchored IDR are predominantly due to the increased contacts of R2 and R3, regions that display residual helical structure. Further, we quantified RHD–IDR interactions driving the compaction and stabilization of the tethered IDR (*SI Appendix*, Fig. S6 and Movie S1). We found that the residues 306 to 351 of the IDR consistently displayed contacts with the linker region of the RHD containing an amphipathic helix (AH_L; see *SI Appendix*, Fig. S6*A*), resulting in IDR compaction. The collapse of the IDR was slower but overall preserved when we altered the interaction strength of the IDR (using $\alpha = 0.1$; *SI Appendix*, Fig. S6*B*) or changed R1, R2, and R3 from helix to coil conformation (*SI Appendix*, Fig. S6*C*). Additionally, we found that transient interactions of hydrophobic residues of the IDR with the membrane lipids (*SI Appendix*, Fig. S6 *Right*) contributed to the overall compact state of the IDR. Two short hydrophobic stretches (280 to 300 and 390 to 400) interacted consistently with POPC lipids, causing the IDR to scaffold over the RHD (*SI Appendix*, Fig. S6 *A*, *Right*).

FAM134B-IDR Induces Membrane Curvature. To determine whether the structure and dynamics of membrane-anchored IDRs influence the local membrane shape, we monitored the local height of the bilayer, $h(x, y)$, and its associated curvature field, $H(x, y)$, under the influence of periodic boundary conditions (*Methods*). We used membrane containing $KALP_{25}$ and RHD without anchored IDRs as negative and positive controls, respectively. As expected, the bilayer with embedded $KALP_{25}$ remained flat with minimal height fluctuations (Fig. 4*A*). However, when linked to the IDR ($KALP_{25}$–IDR), we found a slight bump in the height profile of the membrane consistent with the induction of a small positive membrane curvature (Fig. 4*B*). This indicated that the IDR could induce positive membrane curvature locally. We also confirmed our previous computations (17) that the RHD alone perturbed the bilayer by causing a local bulge with strong positive curvature (Fig. 4*C*). The membrane-shaping effect was greatly amplified upon tethering the IDR to the RHD, resulting in a distinct membrane bulge (Fig. 4*D*).

To further test the role of IDRs in inducing membrane curvature, we lowered the barrier for local bulging by increasing

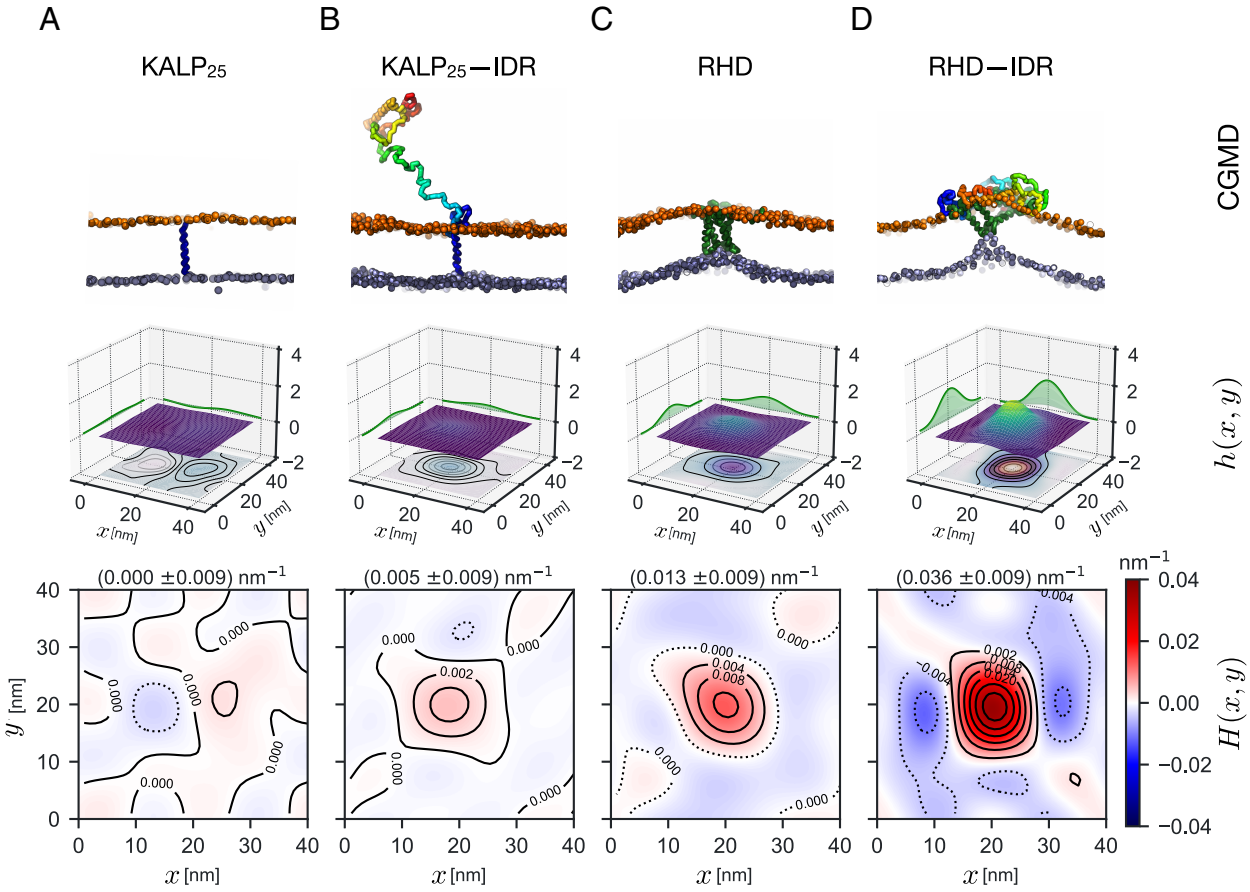

Fig. 4. Membrane-anchored IDRs induce membrane curvature in coarse-grained MD simulations. Square bilayer patches (38 × 38 nm^2) under periodic boundary conditions containing (*A*) $KALP_{25}$ (negative control), (*B*) $KALP_{25}$–IDR, (*C*) FAM134B-RHD (positive control), and (*D*) RHD–IDR perturb bilayer structure differently. (*Top*) Side view snapshots at 5 μs showing the characteristic local membrane shape represented by lipid head groups from both leaflets (orange and blue PO4 beads) around the membrane inclusion. (*Middle*) Local membrane shape is approximated by a height function $h(x,y)$ of the midplane (height contour map along *xy* plane). Projections onto the *xz* and *yz* planes show the shape profile around the inclusion. (*Bottom*) Contour maps of the averaged curvature profiles $H(x,y)$ for each system show the extent of curvature induction around the inclusion centered in the box. The maximum value of curvature fields $\langle H_{max} \rangle$ and ± SD is shown at the *Top*. Midplane $h(x,y)$ and corresponding $H(x,y)$ are computed by fitting 500 individual frames at 2-ns intervals over the last 1 μs of representative trajectories.

the bilayer asymmetry (18) ($\Delta N = N_{upper} - N_{lower} = [100, 300, 500]$; *SI Appendix*, Fig. S7). We found that the RHD–IDR-induced membrane curvature increased with the extent of bilayer asymmetry. This pattern was also observed for RHD alone but moderately. By contrast, the presence of other proteins did not show a steady increase in the bilayer curvature with increasing bilayer asymmetry (*SI Appendix*, Fig. S7).

We further elucidated the role of the IDR in direct membrane remodeling by reanalyzing previous experimental results from FAM134B-induced in vitro liposome remodeling (17, 19). In these experiments, we had reconstituted empty liposomes ($d \approx 200$ nm) with purified proteins (GST-tagged FAM134B-RHDs, full-length FAM134B-WT, and FAM134B-17KR mutant, where all 17 RHD sites have K ↦ R mutations) and imaged them by negative-stain transmission electron microscopy (nsTEM; *SI Appendix*, Fig. S8). We found that the FAM134B-WT and the FAM134B-17KR mutant with intact IDRs drastically remodeled larger liposomes into smaller vesicles ($d = 28 \pm 16$ nm and $d = 27 \pm 8$ nm). By comparison, the RHD alone (*SI Appendix*, Fig. S8) retained liposome remodeling behavior ($d = 57 \pm 25$ nm), albeit less than RHDs flanked by IDRs. Our simulations on RHD–IDR are consistent with these observations and explain the difference in the observed size distribution of proteoliposomes.

FAM134B-IDR Senses Membrane Curvature. Next, we determined the intrinsic curvature preference of proteins with and without tethered IDRs by simulating a buckled bilayer under tension (*Methods* and *SI Appendix*, Table S4). The membrane buckle presents a sinusoidal carpet-like folded structure with a range of local mean curvatures ($H(x,y) = -0.07$ to $+0.07$ nm^{-1}) under periodic boundary conditions. By lateral diffusion (17) or dissociation and reassociation (28), membrane-bound proteins preferentially sample different local curvature environments, allowing us to directly quantify their curvature preference (Fig. 5).

In control simulations with the $KALP_{25}$, we observed a slight preference for surfaces with negative mean curvature ($H(x,y) = -0.019$ nm^{-1}; Fig. 5*A*) akin to structures at the bottom of the buckle with negative Gaussian curvature ($K_G \leq 0$; *SI Appendix*, Fig. S9*A*). Consistent with previous computations, we found that the RHD alone strongly preferred regions of high local mean curvature ($H(x,y) = 0.029$ nm^{-1}; Fig. 5*C* and *SI Appendix*, Fig. S9*C*) occupying the top of the membrane buckle ($K_G > 0$ corresponding to ellipsoidal vesicle shapes). Interestingly, by tethering an IDR to the $KALP_{25}$ peptide, we found that the curvature preference of the molecule changed drastically. The $KALP_{25}$–IDR displayed biased diffusion and migrated toward the top of the buckle with a preference for regions with high positive mean curvature ($H(x,y) = 0.021$ nm^{-1}; Fig. 5*B*) akin to

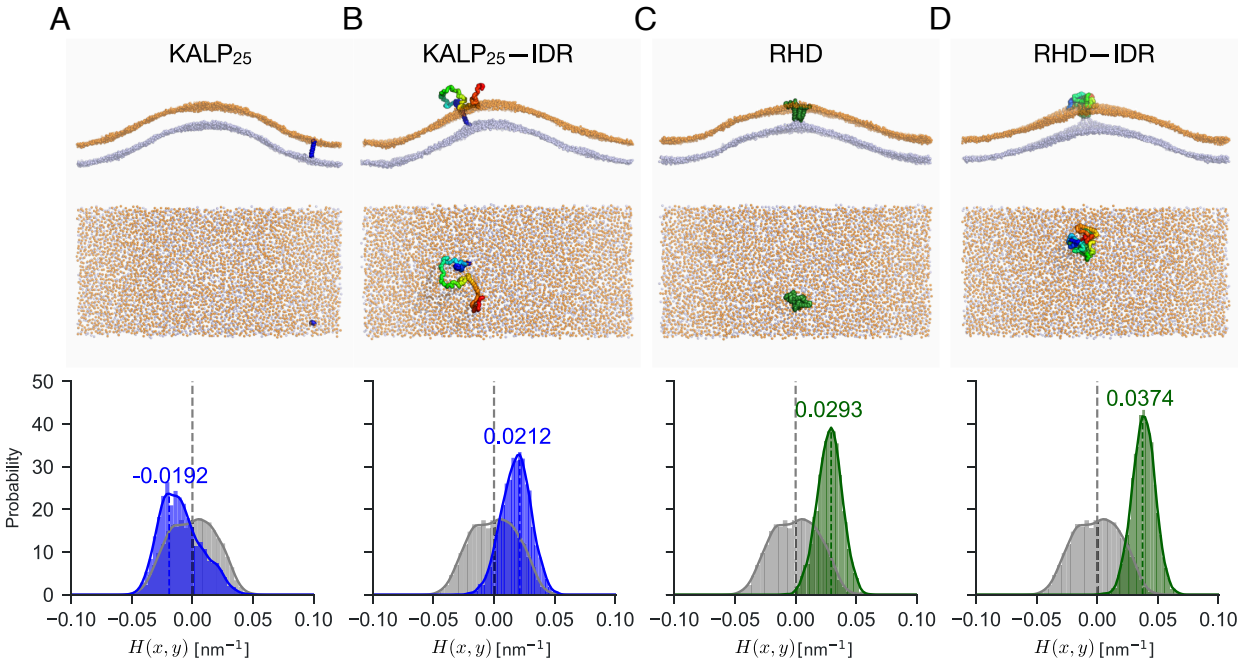

Fig. 5. Membrane-anchored IDRs sense membrane curvature. Rectangular membrane buckles (58 × 27 nm^2) were embedded with proteins. (*A*) $KALP_{25}$ (negative control), (*B*) $KALP_{25}$–IDR, (*C*) FAM134B-RHD (positive control), and (*D*) RHD–IDR were embedded in rectangular membrane buckles (60 × 30 nm^2) and subjected to coarse-grained MD simulations to quantify their curvature preferences. (*Top*) Snapshots (side and top views) at the end of the 10 μs runs show the preferred position of the protein along the buckle. (*Bottom*) Histograms of the mean curvature $H(x,y)$ sampled by the center-of-mass positions of the proteins (transmembrane regions only, $KALP_{25}$ in blue; RHD in green) indicate curvature preference along the buckle. The IDR-containing proteins sample regions of high mean curvature and preferentially occupy the top of the buckle. For reference, the distribution of local mean curvature values on the empty buckled membrane (gray) was estimated by random sampling of points in the *xy* plane, ignoring small curvature corrections. The time-averaged values of $H(x,y)$ are also highlighted.

the tubular geometry on top of the buckle ($K_G \geq 0$; *SI Appendix*, Fig. S9*B*). Upon tethering the IDR to the RHD, we found that the curvature profile of the buckle altered more swiftly, causing an enhanced preference for positively curved surfaces on top of the buckle ($H(x,y) = 0.037$ nm^{-1}; Fig. 5*D*). This enhanced curvature preference exceeds the RHD's curvature preference, is bidirectional ($K_G \gg 0$; *SI Appendix*, Fig. S9*D*), and further deforms the top of the buckle.

FAM134B-IDR Boosts RHD-Mediated Membrane Budding. Motivated by the above findings, we investigated the impact of membrane-anchored IDRs on RHD-induced budding. Previously, we probed the effect of RHD clustering on membrane shape (18). As in this earlier study, we modulated the kinetic barrier and energetic driving force for forming highly curved bud shapes by varying the bilayer leaflet asymmetry and protein concentration. We initiated simulations from flat metastable asymmetric bilayers (2 to 13% leaflet asymmetry) containing different numbers $n_{\mathrm{Prot}} = [3,\ 6,\ 9]$ of $KALP_{25}$ peptides, $KALP_{25}$–IDRs, RHDs, or RHD–IDR molecules (*Methods* and *SI Appendix*, Fig. S10 and Table S5). Tracking individual proteins (*z*-position) and their interactions (clusters) along with the box width (L_x) in these simulations provided an excellent set of order parameters to characterize protein clustering, membrane shape changes, and other features associated with spontaneous budding (Fig. 6).

We found that bilayers containing $KALP_{25}$ peptides or $KALP_{25}$–IDRs did not induce membrane budding under all simulation conditions (Fig. 6 *A* and *B* and *SI Appendix*, Fig. S10 *A* and *B* and Table S5 and Movie S2). Consistent with our previous studies, RHDs, and RHD–IDRs induce spontaneous membrane buds by clustering (Fig. 6 *C* and *D* and Movie S2). The number of budding events within the three replicates increased with protein concentration and bilayer asymmetry (n_{Prot} and ΔN; *SI Appendix*, Fig. S10 C and *D* and Table S6). For RHDs alone in the absence of IDRs, we found infrequent budding that occurred at a much slower rate ($N_{\mathrm{buds}} = 1/3$; $k_{\mathrm{RHD}} = 20$ ns^{-1}; *SI Appendix*, Fig. S11*A*). By contrast, the RHDs with tethered IDRs induced membrane buds more frequently at faster rates on the MD timescale ($N_{\mathrm{buds}} = 3/3$; $k_{\mathrm{RHD-IDR}} = 57$ ns^{-1}; *SI Appendix*, Fig. S11*B*). Further, nine RHDs were required to induce budding at intermediate leaflet asymmetry (6.5 to 7.5%; $\Delta N = 300$; *SI Appendix*, Fig. S11*A* and Movie S2). By contrast, under the same conditions, six RHD–IDRs were sufficient to induce budding repeatedly (*SI Appendix*, Fig. S11*B*). We express the driving force for membrane budding by measuring the rate from observed waiting times for bud formation (*SI Appendix*, Table S6). We estimate that the IDRs of FAM134B accelerated the kinetics of RHD-mediated spontaneous budding by a factor of 3.3 and 2.0 for bilayers with intermediate ($\Delta N = 300$) and high ($\Delta N = 500$) asymmetry, respectively. In simulations containing multiple copies of RHD–IDRs, we found that IDR dynamics increased inter-protein contacts in the solution phase (*SI Appendix*, Fig. S12*A*). Mapping IDR-IDR interactions from MD simulations identified more frequent contacts of residual helical structures R2 and R3. These contacts promoted RHD-clustering, leading to accelerated kinetics of budding.

At high asymmetry ($\Delta N = 500$), bilayers containing $KALP_{25}$s or $KALP_{25}$–IDRs remained nearly flat, indicating that the $KALP_{25}$ peptide clusters within the bilayer were insufficient to overcome the barrier for budding (*SI Appendix*, Fig. S10 *A* and *B*). Although $KALP_{25}$–IDRs did not induce spontaneous buds, the solution-phase IDR–IDR interactions promoted faster

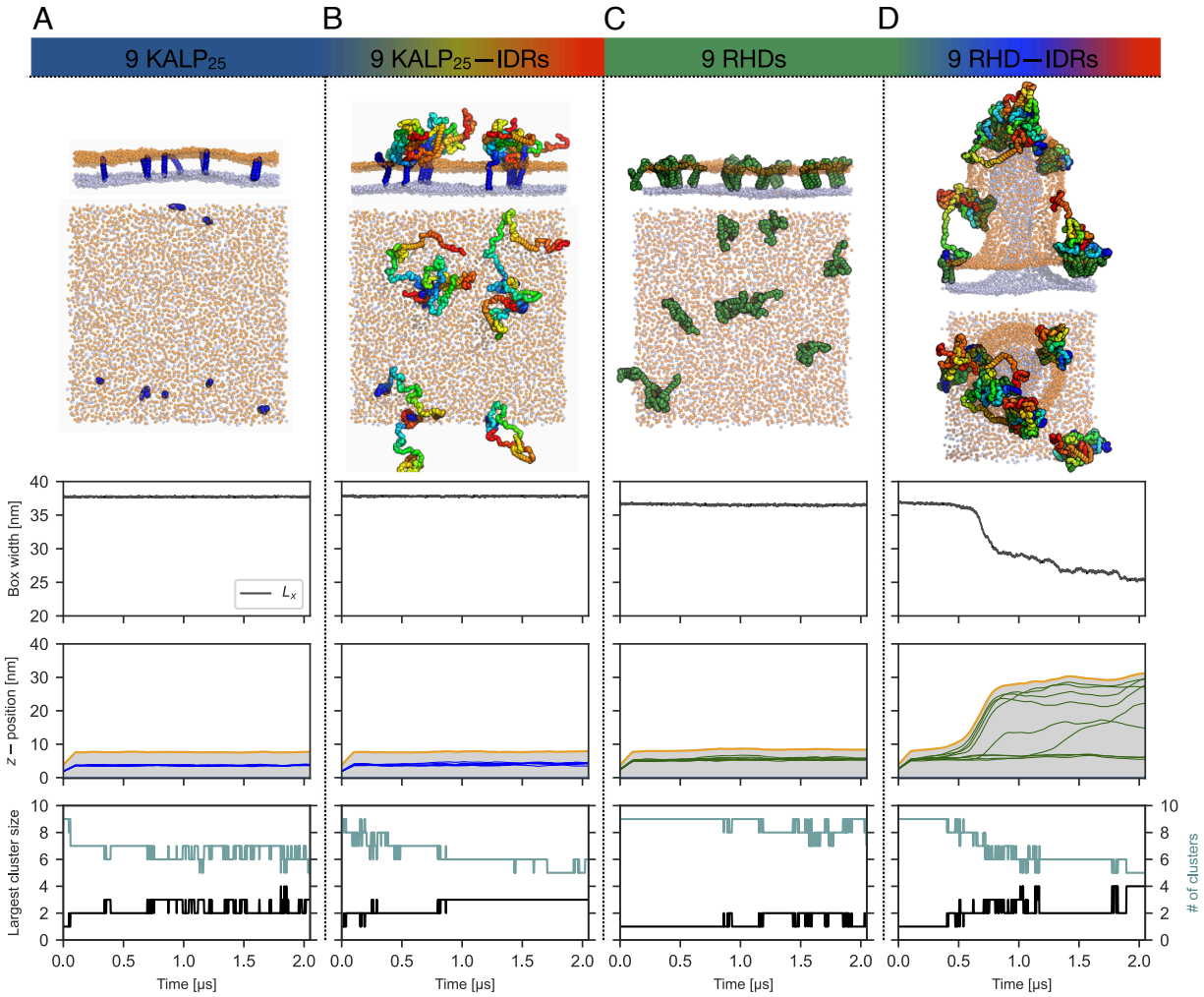

Fig. 6. Membrane-anchored IDRs boost membrane budding. In coarse-grained MD simulations, we embed flat square asymmetric bilayer patches ($\Delta N = 500$; 38×38 nm^2) with nine copies of (*A*) $KALP_{25}$ (negative control), (*B*) $KALP_{25}$–IDR, (*C*) FAM134B-RHD (positive control), and (*D*) RHD–IDR. (*Top*) Snapshots showing side and top views of the organization of proteins at the end of 2 μs runs. (*Middle*) The central two rows display the time traces of order parameters informing on spontaneous membrane budding events. Sharp drops in the box width (L_x) and rapid vertical displacement z of individual proteins (COM positions of transmembrane segments; blue and green lines), along with a rise in the highest points in the bilayer (orange lines) and the intervening range (light gray shaded region), indicate membrane budding. (*Bottom*) The number of segregated protein clusters and the size of the largest protein cluster quantify the extent of clustering, determining the kinetics of budding. IDRs mediate inter-protein interactions and enhance RHD–IDR clustering to induce spontaneous membrane buds faster. We note that on a longer time scale, the RHDs alone also induce membrane budding (*SI Appendix*, Figs. S10 and S11).

protein-clustering (*SI Appendix*, Fig. S12*B*), resulting in local membrane bulges with marginal positive curvatures (*SI Appendix*, Fig. S13). To test whether such structures could drive budding ultimately, we increased the protein surface density from 6,233 molecules per μm^2 to 13,850 molecules per μm^2. We applied slight positive lateral pressure ($P_{xy} = 2$ bar), lowering the barrier for budding (*SI Appendix*, Fig. S14). Despite these favorable conditions, the bilayer with $KALP_{25}$ peptides remained flat and resisted buckling. By contrast, the IDR-IDR interactions of $KALP_{25}$–IDRs broke this metastability by inducing a bulge that then transitioned quickly into a membrane bud, even at low and intermediate leaflet asymmetries (2 to 7.5%; $\Delta N = [100,\ 300]$).

To study the effect of IDR on the autophagic response of FAM134B, we first modeled an IDR variant by deleting the entire segment spanning R1 and R2 (ΔR12 = 265 to 437), shortening the overall IDR length ($L_{IDR} = 64$). The intact IDR ($L_{IDR} = 237$) with this segment displayed protein-protein and protein-membrane interactions, promoting enhanced curvature-mediated sorting of RHDs and RHD-scaffolding behavior. In our simulations of the asymmetric bilayers ($\Delta N = 500$ and $n_{Prot} = 9$), we found that the IDR variant, RHD–IDR$^{\Delta R12}$ displayed aberrant budding behavior in comparison to intact RHD–IDR molecules (*SI Appendix*, Fig. S15 *A* and *B*). RHD–IDR$^{\Delta R12}$ molecules induced fewer budding events spontaneously ($N_{buds} = 9/20$ vs. $N_{buds} = 17/20$) with slower rates of bud formation ($k_{\Delta R12} \leq 0.59\ \mu s^{-1}$ vs. $k_{WT} \leq 0.76\ \mu s^{-1}$).

Motivated by these findings, we assessed the effect of this IDR deletion on selective ER-phagy function in cells (*SI Appendix*, Fig. S15 *C* and *D*). We overexpressed wild-type and deletion constructs of FAM134B in U2OS cells and evaluated the status of the ER fragmentation 24 h after transfection. The full-length protein (WT) and the LIR_{mut} or the RHD alone served as positive and negative controls, respectively (17, 19). A confocal microscopy-based assay confirmed the formation of characteristic autophagic puncta and the induction of relevant ER fragmentation in cells expressing the wild-type protein (*SI Appendix*, Fig. S15 *C* and *D*, column 1). Deletion of the R12 segment from the IDR significantly reduced the number

of puncta per cell (*SI Appendix*, Fig. S15 *C* and *D*, column 2). However, FAM134B-RHD and the FAM134B-LIR$_{mut}$ were still localized in the ER, as shown by the overlap with the calnexin signal (*SI Appendix*, Fig. S15 *C* and *D*, columns 3 to 4). This finding is consistent with our simulations and corroborates the mechanistic understanding of IDR action and amplification of RHD functions during selective ER-phagy.

Discussion

IDRs are ubiquitous in autophagy. Their prevalence in effector proteins during autophagy initiation, autophagosome nucleation, expansion, and maturation provides functional plasticity to distinct molecular processes (29). The abundance of IDRs in established and newly identified selective autophagy receptors, coupled with the existence of LIRs, PTMs, and diverse interaction partners, underscores their central role in autophagy (30). Further, the cytosolic IDRs of membrane receptors exploit their unstructured conformational ensemble, propensity for PTMs, and alternate motif-based binding modes to exert direct control on organellar homeostasis (1).

Modeling IDR ensembles is challenging. Their structural and functional characterization relies heavily on recent advances in experiment (31) and theory (32, 33). In particular, particle-based MD simulations using coarse-grained models offer a powerful means, enabling direct comparison with experimental observables (34). Despite its limitations (35), the Martini force field has proven to be highly efficient for simulating protein-membrane systems (17, 36, 37). However, for several multidomain proteins and IDRs, it might lead to an overestimation of protein-protein interactions (26), resulting in unrealistically compacted regions (38). Current solutions to overcome the stickiness rely on the improvement of interaction models (39, 40) and enhanced sampling (41).

Scaling of the protein-water (42) or protein-protein interactions (27) in the Martini model is required to simulate the correct ensemble properties of IDRs, including correct folding (43), formation of RNA-IDR complexes (44), and the formation of phase-separated condensates by FUS (27). Here, we modeled the IDR of FAM134B using extensive parameterization. By adopting a scaled Martini model optimized against atomistic MD simulations, we provide a refined depiction of the FAM134B-IDR ensemble in solution. By employing hybrid scaling within the same polypeptide, we provide an even more optimized description of membrane-anchored IDRs and their interactions under varied molecular contexts (e.g., tethered to different membrane proteins). This allowed us to exploit the efficiency of the Martini model to study the influence of the IDR on the membrane remodeling capacity of ER-phagy receptors (17–19).

IDR conformations sampled in the coarse-grained simulations ($\alpha = 0.6$) show overlap with all-atom simulations reproducing its conformational landscape. The overall structure and organization of the IDR ensemble, its residual secondary structure, and tertiary interactions are consistent with sequence-based predictions of IDR characteristics (e.g., predicted MoRFs, pLDDTs, and binding sites). Anchoring the IDR to bilayers resulted in a context-dependent sampling of conformations. Consistent with its location in the Das-Pappu diagram (16), the membrane-anchored IDRs display both expanded (KALP$_{25}$–IDR) and compact states (RHD–IDR), highlighting its Janus-like behavior. The preservation of this feature across the majority of ER-phagy receptors and their homologs strongly suggests a significant functional or regulatory role for the IDRs.

The combination of protein disorder and membrane dynamics is central to signaling (2). Membrane-anchored IDRs mediate signal transduction across bilayers, scaffold signaling complexes, and regulate vesicle trafficking, functions central to ER-phagy receptors (1). Our simulations of IDRs anchored to the bilayer perturb local membrane shape, clearly demonstrating IDR-mediated active membrane curvature induction and sensing. We found that IDRs anchored to membranes adopt extended conformations, increasing their hydrodynamic volume (4). Tethering them to flat bilayers also limits the number of accessible conformations, inducing positive membrane curvature through entropic forces (22, 45) as demonstrated for IDRs in epsin, AP180, and amphiphysin (22, 46). Alternatively, IDRs with a net negative charge could be electrostatically repelled by a bilayer containing anionic lipids to induce local membrane bending, reducing overall steric hindrance (23). Phosphorylation of the FAM134B-IDR could also enhance this effect.

Further, at high concentrations, IDRs induce increased lateral pressure, enhancing membrane deformations (47). Steric crowding of IDRs in amphiphysin and epsin induces the formation of buds or tubules (22, 48). In light of simulations of the RHD with the C-terminal IDR, we revisited previous in vitro liposome remodeling assays (17, 19) and found that full-length FAM134B-WT and the FAM134B-17KR mutant with preserved C-terminal IDRs are much more efficient in remodeling liposomes (≈56% smaller liposomes), highlighting the importance of IDRs in accentuating RHD-mediated curvatures. Consistent with these observations, we found that FAM134B-IDR mediated protein-protein interactions, enhancing the kinetics of receptor clustering and membrane budding. Often, the entropic, electrostatic, and crowding mechanisms collectively influence the structural state of the IDR, thereby modulating local membrane curvature and large-scale remodeling (25).

FAM134B-IDR plays a pivotal role in magnifying membrane remodeling during ER-phagy (Fig. 7). The IDR conformations and emergent ensemble properties are directly influenced by tethered RHDs (Fig. 7*A*). Further, phosphorylation and ubiquitination of specific residues could aid in reversible switching between expanded and compact IDR conformations (Fig. 7*B*). The entropic force generated by the surface tethering is sequence-encoded and fine-tuned by the immediate environment. The interplay of variable conformational entropy, direct membrane interactions, and RHD scaffolding amplifies curvature induction and sensing with significant implications across various steps of selective ER-phagy (Fig. 7*C*). The LIR motif, located within the conformationally variable IDR, recruits hATG8 presumably through fly-casting mechanisms. Fuzzy binding modes of multiple LIR-LDS interactions heighten avidity, stabilizing molecular bridges across the ER and the phagophore membrane. Additionally, the Janus-like behavior of the IDRs, along with IDR-IDR interactions, intensifies volume exclusion effects, increasing the effective receptor concentration and expediting membrane budding (Fig. 7*D*).

In conclusion, we identified a role for the IDRs in ER-phagy receptors. We demonstrated how context-dependent ensemble properties of the IDR influence local membrane properties to induce and sense positive membrane curvature actively. Coupled with established RHD functions (17, 18), the IDRs enhance receptor clustering and hasten membrane budding, thereby augmenting selective ER-phagy. It remains to be seen how multiple regulatory mechanisms coupled to IDR conformational dynamics are actively exploited under varied physiological and stress conditions to modulate overall autophagic flux.

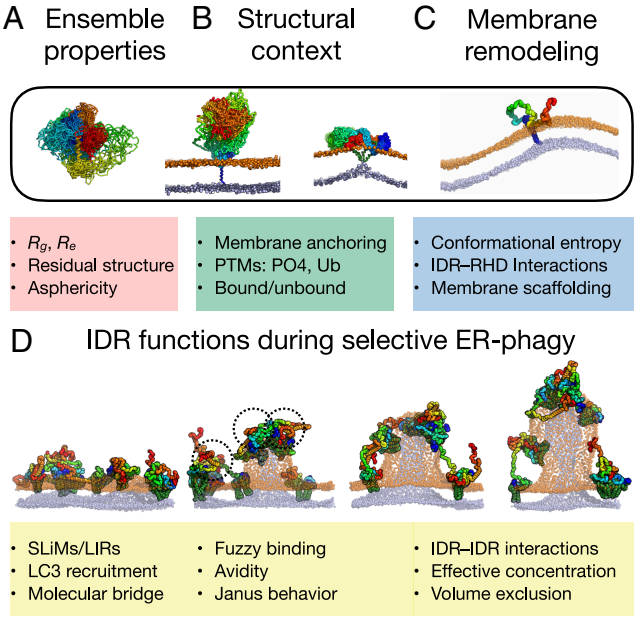

Fig. 7. IDRs amplify membrane remodeling during ER-phagy. (*A*) Ensemble properties of the FAM134B-IDR are determined not only by its unique sequence features but are also strongly influenced by the diverse (*B*) molecular, structural contexts and various cellular physiological states. (*C*) IDRs anchored to the RHDs of individual receptors, driven by conformational entropy, can actively induce and sense local bilayer curvature, enhancing the RHD functions. (*D*) The Janus-like behavior of the IDR affects conformational sampling and could influence the fuzzy LIR–LDS binding to hATG8 proteins to enhance avidity during phagophore recruitment. Further, solution-phase IDR–IDR interactions increase effective RHD concentration to drive faster clustering and budding, amplifying large-scale membrane remodeling processes during ER-phagy.

Methods

Sequence Analysis of IDRs in ER-Phagy Receptors. IDR segments of well-known ER-phagy receptors: FAM134B, TEX264, SEC62, RTN3, and CCPG1 (*SI Appendix*, Table S1) were annotated using D^2P^2 (49), a consensus predictor combining nine different IDR prediction algorithms (https://d2p2.pro/; *SI Appendix*, Figs. S1 and S2*A*). Homologs for all ER-phagy receptors were obtained using psi-BLAST (50) searches against the NR database. Hits ($n = 500$ each) were filtered with an E-value cutoff of 10^{-4}, sequence identity range of 30 to 90%, and a query coverage of $\geq$70%. IDR annotations for the homologs were then mapped from query-hit alignments to compute the fraction of positive (f_+; K and R), negative (f_-; D and E), total charged residues (Fraction of Charged Residues $= f_+ + f_-$), and the net charge per residue (NCPR $= |f_+ - f_-|$). Probability distributions of charge properties of IDR were mapped onto the Das-Pappu plot to identify the most plausible conformational state (i.e., polar tracts, polyampholytes, or polyelectrolytes) (16).

Structural Model for FAM134B–IDR. Previously, the structure of FAM134B obtained from extensive modeling and simulations was limited to the membrane-bound RHD (17). We used AlphaFold2 (https://alphafold.ebi.ac.uk/) to obtain an initial structural model for the C–terminal IDR (residues 261 to 497) of FAM134B (51). The local per-residue confidence score (pLDDT: predicted Local Distance Difference Test) and PAE (Predicted Alignment Error) were used to assess any residual secondary structures (e.g., helical stretches with pLDDT $\geq$ 50%) and tertiary contacts along the IDR and compared with sequence-based predictions of molecular recognition features (MoRFs) from D^2P^2 (*SI Appendix*, Fig. S2). We connected the IDR structure to the C terminus of $KALP_{25}$ peptide and RHD (residue 80 to 260) to model membrane-anchored molecules, $KALP_{25}$–IDR and RHD–IDR, respectively. These models were then energy minimized to remove steric clashes and equilibrated under appropriate solvent conditions.

Molecular Dynamics Simulations. All MD simulations, including energy minimization, equilibrations (NVT and NPT), and production runs, were performed with *GROningen MAchine for Chemical Simulations (GROMACS)* v2021.5 (52). A summary of all the MD simulations performed in this study is provided in *SI Appendix*, Tables S2–S5. MD simulations of various protein systems were performed in solution (150 mM NaCl), embedded in flat bilayers (symmetric and asymmetric), and embedded in buckled bilayers to study the IDR conformational dynamics, IDR-induced curvature induction, sensing, and large-scale membrane remodeling.

The AF model of the IDR of FAM134B was used as an initial structure to obtain the IDR conformational ensemble in the solution. The IDR in dilute solution was modeled by first centering the IDR in a large periodic dodecahedron box with a distance of 4 nm between the protein and the box edge and then solvating it with TIP3P water containing 150 mM NaCl to allow extensive structural rearrangements. We used the CHARMM36m force field (53) for atomistic MD simulations. Electrostatic interactions were modeled with particle mesh Ewald summation and a real-space cutoff of 1.2 nm (54). The LINear Constraint Solver (LINCS) algorithm was used to constrain covalent bonds between hydrogen and heavy atoms (55). The Verlet cutoff scheme and the force-switch modifier were used for van der Waals forces with a cutoff of 1.2 nm. The system was first energy-minimized using the steepest descent algorithm and then equilibrated with position restraints on backbone heavy atoms ($F = 1{,}000$ kJ mol^{-1} nm^{-2}) under NPT conditions of constant pressure and temperature, respectively. The system temperature was maintained at 310 K by a Nosé-Hoover thermostat (56–58) with a coupling constant $\tau_T = 1.0$ ps. The system pressure was maintained at 1 bar using the isotropic Parrinello–Rahman barostat (59) with a coupling constant of $\tau_P = 1.0$ ps, and a compressibility of 4.5×10^{-5} bar^{-1}. Production runs using a 2 fs timestep for 1 μs were then initiated for 2 replicates with different initial velocities to assess the IDR conformational dynamics.

We used the Martini 2.2 model (37) for coarse-grained molecular dynamics (CGMD) simulations. Four different protein–membrane systems were built and simulated in flat and buckled bilayers viz., i) $KALP_{25}$, a transmembrane helical peptide spanning the bilayer (negative control), ii) $KALP_{25}$–IDR, where the N terminus of the IDR is tethered to the $KALP_{25}$, iii) RHD of FAM134B (positive control) (17), and iv) RHD–IDR, where the N terminus of the IDR is linked to the C terminus of the RHD. Initial all-atom models were first assembled for these four protein systems from individual fragment structures (i.e., $KALP_{25}$, RHD, and IDR) and then converted to coarse-grained representation using the *martinize.py* script (v2.6) (36). The local secondary structure of the RHD and the $KALP_{25}$ peptide was preserved by adding backbone constraints obtained from DSSP assignments (60). The CG models were then embedded in model bilayers made of 1-palmitoyl-2-oleoyl-sn-glycero-3-phosphocholine (POPC) lipids using *insane.py* (41), followed by solvation using CG water along with 150 mM NaCl.

In all coarse-grained MD simulations, long-range electrostatic interactions were treated using a reaction field with a Coulomb cutoff of 1.1 nm and a dielectric constant ϵ_{rf} of 15. Van der Waals interactions were modeled with a cutoff of 1.1 nm, using the Verlet cutoff scheme and the potential-shift-Verlet modifier. Two rounds of steepest-descent energy minimizations (3,000 steps each) were performed, first using a softcore potential, followed by an energy minimization without any position restraints. Systems were then equilibrated under NVT conditions with the velocity-rescale thermostat (61) at 310 K ($\tau_T = 1.0$ ps), followed by 5-step NPT equilibrations with increasing timesteps (dt=[1, 2, 5, 10, 20] fs) using the Berendsen barostat (62) at 1 bar ($\tau_P = 12.0$ ps) with a compressibility of 3.0×10^{-4}. During the initial two equilibration steps, position restraints were applied to the protein backbone (BB) beads. Additionally, the phosphate (PO4) beads of POPC lipids were weakly restrained along the *z*-axis to prevent out-of-plane fluctuations of the lipids. The position restraints on BB and PO4 beads were gradually removed during the last NPT equilibration step. Production runs were carried out using a 20 fs timestep with the velocity-rescale thermostat (61) and the Parrinello–Rahman barostat (59).

To study the curvature sensing by IDR-containing proteins, buckled membrane systems were built by embedding the four different protein molecules in a pre-equilibrated POPC bilayer buckle. The initial shape of the membrane buckle was obtained using *Lipid-Wrapper* (63) and equilibrated to form a continuous carpet-like folded membrane along the *x*-axis in a fixed *xy*-plane (57×28 nm^2)

under periodic boundary conditions. The proteins were initially placed in a region with low mean curvature, i.e., $H(x, y) \simeq 0$ nm^{-1} followed by system equilibration (NPT conditions: 1 bar; 310 K; anisotropic barostat) and production runs (up to 10 μs) to quantify curvature preferences.

To study protein-induced spontaneous budding in simulations, we used flat asymmetric bilayers varying the copy number ($n_{\text{Prot}} = [1, 3, 6, 9]$ molecules) of different membrane proteins. Proteins were arranged in a square grid, ensuring each protein was separated from its nearest neighbor by approximately 10 nm. We varied relative asymmetries of POPC bilayers (∼2%, ∼7% and ∼12%) by changing the $\Delta N = N_{\text{upper}} - N_{\text{lower}}$, i.e., the difference in the number of lipids between the upper and the lower leaflets ($\Delta N = [0, 100, 300, 500, 700]$) using *insane.py* (41). Production runs were performed for three replicates (NPT conditions: 1 bar; 310 K; semi-isotropic barostat) for 5 μs. Additional 20 replicates were performed for RHD–IDR and RHD–IDR$^{\Delta R12}$ to quantify the effect of IDR on membrane budding.

Rescaling Protein–Protein Interactions. To reproduce the correct ensemble of IDR conformations sampled using the Martini models, the protein–protein Lennard-Jones (LJ) interactions were rescaled following a previously implemented method (27). The parameter α scales the well-depth (ϵ) of the protein–protein LJ potential, $\epsilon_\alpha = \epsilon_0 + \alpha\left(\epsilon_{\text{original}} - \epsilon_0\right)$, such that $\alpha = 0$ corresponds to repulsion-dominated interaction in the Martini model, $\epsilon_0 = 2$ kJ/mol, and $\alpha = 1$ recovers the full interaction of the Martini force field, $\epsilon_0 = \epsilon_{\text{original}}$. This procedure was previously used to model IDR dynamics, formation of phase-separated condensates (27) and demonstrate the role of ubiquitination in RHD-clustering on bilayers (19). Multiple simulations using rescaled PPI at various α-values were performed to optimize it for the IDR of FAM134B. The conformational landscape of IDR ensembles in solution was then compared with atomistic MD simulations to obtain an optimal value ($\alpha = 0.6$). To model the interactions of structured and intrinsically disordered segments within the same polypeptide chain, we used hybrid scaling with two different ϵ_α for self-interactions. ϵ_1 modeled the LJ interactions within the folded/structured region (e.g., KALP$_{25}$/RHD), and $\epsilon_{0.6}$ for interactions within the IDR. LJ parameters for cross-interactions between folded or structured and IDR segments were obtained using Lorentz-Berthelot combination rules, $\epsilon_{ij} = \sqrt{\epsilon_i \epsilon_j}$ (64). The IDR interactions with all other molecules (lipids and solvent) were unchanged corresponding to $\epsilon_{1.0}$ (65).

Backmapping Coarse-Grained Structures. CG structures of IDR ensembles were backmapped to all-atom resolution for computing ensemble properties of the IDR before comparisons with atomistic MD simulations. Atomistic models were obtained using *backward.py* script (66) with appropriate CHARMM36m topology, and energy minimized using the default protocol. Atomistic models of KALP$_{25}$–IDR and RHD–IDR from CGMD simulations were also obtained for computing hydrodynamic properties.

IDR Ensemble Properties. The IDR from various MD simulations in their varied molecular and structural contexts were characterized by computing their ensemble properties. The radius of gyration (R_g), end-to-end distances (R_e), residue-wise local secondary structure assignments, and root mean square fluctuations (RMSF) for the MD trajectories were computed using the *gmx* functions (implemented in *GROMACS* package) *gyrate*, *distance*, *do_dssp*, and *rmsf*, respectively. The local secondary structure probability of the IDR was obtained by counting the relative frequency of α-helix (P_{H}), β-strand (P_{S}) or coil-like (P_{C}) conformations assigned to each residue over the entire atomistic MD trajectory.

Free energy landscapes for backmapped IDR ensembles in solution and membrane-anchored configurations were obtained from the sampled distributions $p(R_g, R_e)$ as $F(R_g, R_e) = -\ln p(R_g, R_e)$ in units of kcal mol^{-1}. Free energy surfaces were computed on concatenated equilibrium MD trajectories of multiple replicates obtained using the polystat function of *GROMACS*.

The hydrodynamic properties of the IDR, such as asphericity, translational hydrodynamic radius (R_T), and rotational hydrodynamic radius (R_R), for the backmapped MD trajectories of the IDR in solution, tethered to KALP$_{25}$ and RHD were estimated with the *HullRad* (67). Moreover, the convex hulls were visualized using *Display_hull3.py* script (67).

Contact Maps. Contact maps for IDR–IDR, IDR–KALP$_{25}$, and IDR–RHD interactions were obtained using *in-house* scripts implementing *MDAnalysis* (68). The residue-wise interactions between two groups, A and B, were estimated for each frame of the trajectory such that $\text{AB}_{\text{cnts}} = \sum_{i\in A}\sum_{j\in B}\sigma(|r_{ij}|)$, where the summation extends over heavy-atom positions of interacting residues (i, j), and $\sigma(|r_{ij}|) = 1 - [0.5 - 0.5(\tanh((|r_{ij}| - r_c)/a))]$, is a smooth sigmoidal counting function that limits contacts below a cutoff distance, r_c. We used $r_c \leq 5$ Å with $a = 0.5$ Å for atomistic systems and $r_c \leq 10$ Å with $a = 1.0$ Å for coarse-grained systems, respectively.

Estimating Membrane Curvatures. Membrane shapes were characterized by quantifying local bilayer properties using a modified version of *MemCurv* (https://github.com/bio-phys/MemCurv) (17). The MD trajectories were post-processed to align all frames such that the protein molecule was centered and oriented parallel to the *x*-axis ($\vec{P} \parallel L_x$). We used the long axis of the central amphipathic helix, (AH_{L}) within the RHD to define its in-plane orientation $\vec{P}$. This ensured the removal of effects arising from the protein's in-plane rotational and translational diffusion. The shape of the bilayer is characterized by a height function $h(x, y)$ of the midplane using a Monge parameterization and approximated by an optimized 2D Fourier function as implemented in *MemCurv* (17). The local height $h(x, y)$ was then used to estimate the local shape operator $\mathbf{S}(x, y)$, which embodies all the curvature properties of the membrane surface. Local directional curvatures (k_1 and k_2), the mean curvature, $H = \text{Tr}(\mathbf{S})/2$, and the Gaussian curvature, $K_{\text{G}} = \det(\mathbf{S})$ are computed for the protein center-of-mass (COM) positions along the membrane by computing the eigenvalues, the trace, and the determinant of the local shape operator $\mathbf{S}(x, y)$, as implemented in MemCurv, respectively. Computations were performed by fitting PO4 beads for every frame to obtain a height profile. The $H(x, y)$ could then be computed for 40×40 grid (width = 1 nm) using *MemCurv*. $h(x, y)$ and $H(x, y)$ were averaged over 500 frames spanning the last 1 μs of the representative trajectories.

For buckled membranes, the lateral diffusion of the protein was tracked by measuring its COM positions along with local shape changes of the buckle, following the original version of *MemCurv* (17). The local shape operator $\mathbf{S}(x, y)$ was calculated as previously described in order to extract values of $k_1, k_2, H(x, y)$, and $K_{\text{G}}(x, y)$.

Analysis of Membrane Budding and Protein Clustering. Order-parameters were used to monitor the spontaneous membrane budding of asymmetric bilayers containing different proteins. Sudden drastic changes in the time series of box width (L_x) provided excellent readout on budding. The average waiting time, $\langle t\rangle = (t_1 + t_2 + t_3)/3$, for a 50% drop in L_x from 3 independent replicates were used to estimate the rate of budding $k = 1/\langle t\rangle$ for each protein–membrane system. To ascertain the role of proteins and the associated shape transition into a bud-like geometry, the projection of the center-of-mass of the protein BB beads and the PO4 beads of both leaflets along the *z*-axis was monitored. This provides a way to track the proteins along the bud shape relative to the highest and lowest points during the budding transition. Further, in MD simulations containing multiple protein copies, a pair-wise inter-protein distance matrix was defined using COM positions of individual proteins along the *xy* plane for each simulation frame. Hierarchical clustering of this matrix with single-linkage and cutoff distance of 10 nm was used to estimate the total number of clusters and the size of the largest protein cluster in each frame of the trajectory. Monitoring the time series of cluster sizes provided information on the role of IDR-mediated protein clustering and associated shape changes in membranes. Further, contact maps of residue-wise IDR–IDR interactions were also estimated for each interprotein pair and averaged over the entire trajectory to map the most frequent IDR contact sites during budding.

Cell Culture and Fluorescence Microscopy. Plasmids with FAM134B-IDR variants: full-length (WT), ΔR12 (Δ265 to 437), RHD (90 to 264), and LIR_{mut} (453 to 458) for mammalian cell-line expression were obtained from either previous

studies or by subcloning FAM134B Orf, fused with the HA tag at the N terminus. (*SI Appendix*, Table S7). U2OS cells (American Type Culture Collection, HTB-96) were cultivated in standard Dulbecco's Modified Eagle Medium (DMEM) supplemented with 10% fetal calf serum (Gibco) and 100 μg/ml penicillin and streptomycin (Thermo Fisher Scientific). Cells were maintained at 37 °C with 5% CO_2 and regularly monitored for *mycoplasma* using the LookOut-*Mycoplasma*-qPCR detection kit (SIGMA).

For immunofluorescence (IF) experiments, cells were then grown on 12 mm glass coverslips for 24 h at 37 °C and transfected with 0.5 μg of various plasmids (*SI Appendix*, Table S7) using the Turbofect reagent (Thermo Fisher Scientific). Primary antibodies, anti-HA (Roche: #11867423001; dilution 1:500) and anti-calnexin (AbCam: #Ab22595; dilution 1:500), were diluted in 5% FBS/0.1% saponin in PBS (1X) and incubated with cells overnight at 4 °C. Secondary antibodies were then added and incubated for 1 h at room temperature: anti-rabbit Alexa 555 (Life Technologies A31572, Ober-Olm, Germany; dilution 1:500), anti-rat Alexa 488 (Life Technologies A21208, Ober-Olm, Germany; dilution 1:500), Alexa Flour 647-conjugated Phalloidin (Cell Signaling: #8940, dilution 1:500) and nuclear dye 4′,6-diamidino-2-phenylindole (DAPI). Immunofluorescent images were acquired with a Leica SP8 laser-scanning microscope fitted with a x63 oil-immersion lens. Representative images were obtained from duplicate IF experiments and analyzed for ER-associated FAM134B-induced punctate structures using the CellProfiler (69). Automatic thresholding of DAPI- and phalloidin-stained images was used to define individual cells and trace the cell body. For each sample, representative images were analyzed for the distribution of the distinct number of FAM134B-positive punctate structures (# of puncta per cell; $n \geq 50$ transfected cells). Puncta distributions were checked for normality using Shapiro–Wilkson and KS tests and then compared across different samples using nonparametric one-way ANOVA tests.

Data, Materials, and Software Availability. All algorithms and computer codes used are described and cited appropriately in *Methods*. Raw trajectory files supporting the data can be accessed from the ref. 70. All other data are included in the manuscript and/or supporting information.

ACKNOWLEDGMENTS. This work is partially supported by the Cluster project EnABLE, funded by the Hessian Ministry for Science and Arts, and the Collective Research Center project on Selective Autophagy, Deutsche Forschungsgemeinschaft Project-ID 259130777-SFB1177 (to I.D., G.H., and R.M.B.). S.A.P.-C. and K.L. acknowledge funding from the EnABLE cluster and the SFB-1177 consortia, respectively. B.M. and I.D. are also supported by the European Research Council (grant ER-REMODEL). G.H. thanks the Max Planck Society for support. We thank the Center for Supercomputing, Goethe University Frankfurt, for computing time on the Goethe-Hochleistungsrechenzentrum cluster. We also thank Arghya Dutta and Lukas Stelzl for the fruitful discussions and David Krause for system administration.

Author affiliations: [a]Goethe University Frankfurt, School of Medicine, Institute of Biochemistry II, Frankfurt am Main 60590, Germany; [b]Goethe University Frankfurt, Buchmann Institute for Molecular Life Sciences, Riedberg Campus, Frankfurt am Main 60438, Germany; [c]International Max Planck Research School on Cellular Biophysics, Max-von-Laue-Strasse 3, Frankfurt am Main 60438, Germany; [d]Max-Planck Institute of Biophysics, Department of Theoretical Biophysics, Frankfurt am Main 60438, Germany; and [e]Goethe University Frankfurt, Department of Physics, Institute of Biophysics, Frankfurt am Main 60438, Germany

1. R. Van Der Lee *et al.*, Classification of intrinsically disordered regions and proteins. *Chem. Rev.* **114**, 6589–6631 (2014).
2. J. Cornish, S. G. Chamberlain, D. Owen, H. R. Mott, Intrinsically disordered proteins and membranes: A marriage of convenience for cell signalling? *Biochem. Soc. Trans.* **48**, 2669–2689 (2020).
3. G. Tesei, T. K. Schulze, R. Crehuet, K. Lindorff-Larsen, Accurate model of liquid-liquid phase behavior of intrinsically disordered proteins from optimization of single-chain properties. *Proc. Natl. Acad. Sci. U.S.A.* **118**, e2111696118 (2021).
4. J. C. Stachowiak *et al.*, Membrane bending by protein-protein crowding. *Nat. Cell Biol.* **14**, 944–949 (2012).
5. O. N. Yogurtcu, M. E. Johnson, Cytosolic proteins can exploit membrane localization to trigger functional assembly. *PLoS Comput. Biol.* **14**, e1006031 (2018).
6. B. A. Shoemaker, J. J. Portman, P. G. Wolynes, Speeding molecular recognition by using the folding funnel: The fly-casting mechanism. *Proc. Natl. Acad. Sci. U.S.A.* **97**, 8868–8873 (2000).
7. M. K. Araya, Y. Zhou, A. A. Gorfe, Remodeling of the plasma membrane by surface-bound protein monomers and oligomers: The critical role of intrinsically disordered regions. *J. Memb. Biol.* **255**, 651–663 (2022).
8. P. E. Wright, H. J. Dyson, Intrinsically disordered proteins in cellular signalling and regulation. *Nat. Rev. Mol. Cell Biol.* **16**, 18–29 (2015).
9. J. A. Ditlev, Membrane-associated phase separation: Organization and function emerge from a two-dimensional milieu. *J. Mol. Cell Biol.* **13**, 319–324 (2021).
10. F. Reggiori, M. Molinari, ER-phagy: Mechanisms, regulation, and diseases connected to the lysosomal clearance of the endoplasmic reticulum. *Phys. Rev.* **102**, 1393–1448 (2022).
11. F. Xu *et al.*, COPII mitigates ER stress by promoting formation of ER whorls. *Cell Res.* **31**, 141–156 (2021).
12. S. Ferro-Novick, F. Reggiori, J. L. Brodsky, ER-phagy, ER homeostasis, and ER quality control: Implications for disease. *Trends Biochem. Sci.* **46**, 630–639 (2021).
13. J. Li, E. Gao, C. Xu, H. Wang, Y. Wei, ER-phagy and microbial infection. *Front. Cell Dev. Biol.* **9**, 771353 (2021).
14. C. A. Hübner, I. Dikic, ER-phagy and human diseases. *Cell Death Differ.* **27**, 833–842 (2020).
15. A. Gubas, I. Dikic, ER remodeling via ER-phagy. *Mol. Cell* **82**, 1492–1500 (2022).
16. R. K. Das, R. V. Pappu, Conformations of intrinsically disordered proteins are influenced by linear sequence distributions of oppositely charged residues. *Proc. Natl. Acad. Sci. U.S.A.* **110**, 13392–13397 (2013).
17. R. M. Bhaskara *et al.*, Curvature induction and membrane remodeling by FAM134B reticulon homology domain assist selective ER-phagy. *Nat. Commun.* **10**, 2370 (2019).
18. M. Siggel, R. M. Bhaskara, M. K. Moesser, I. Dikić, G. Hummer, FAM134B-RHD protein clustering drives spontaneous budding of asymmetric membranes. *J. Phys. Chem. Lett.* **12**, 1926–1931 (2021).
19. A. González *et al.*, Ubiquitination regulates ER-phagy and remodelling of endoplasmic reticulum. *Nature* **618**, 394–401 (2023).
20. H. Foronda *et al.*, Heteromeric clusters of ubiquitinated ER-shaping proteins drive ER-phagy. *Nature* **618**, 402–410 (2023).
21. C. Has, P. Sivadas, S. L. Das, Insights into membrane curvature sensing and membrane remodeling by intrinsically disordered proteins and protein regions. *J. Membr. Biol.* **255**, 237–259 (2022).
22. W. F. Zeno *et al.*, Synergy between intrinsically disordered domains and structured proteins amplifies membrane curvature sensing. *Nat. Commun.* **9**, 4152 (2018).
23. W. F. Zeno *et al.*, Molecular mechanisms of membrane curvature sensing by a disordered protein. *J. Am. Chem. Soc.* **141**, 10361–10371 (2019).
24. W. Snead, C. Hayden, A. Gadok, P. Rangamani, J. Stachowiak, Membrane fission by protein crowding. *Biophys. J.* **112**, 327a (2017).
25. J. R. Houser *et al.*, Molecular mechanisms of steric pressure generation and membrane remodeling by disordered proteins. *Biophys. J.* **121**, 3320–3333 (2022).
26. A. C. Stark, C. T. Andrews, A. H. Elcock, Toward optimized potential functions for protein-protein interactions in aqueous solutions: Osmotic second virial coefficient calculations using the Martini coarse-grained force field. *J. Chem. Theory Comput.* **9**, 4176–4185 (2013).
27. Z. Benayad, S. von Bülow, L. S. Stelzl, G. Hummer, Simulation of FUS protein condensates with an adapted coarse-grained model. *J. Chem. Theory Comput.* **17**, 525–537 (2020).
28. S. Rao *et al.*, Three-step docking by WIPI2, ATG16L1, and ATG3 delivers LC3 to the phagophore. *Sci. Adv.* **10**, eadj8027 (2024).
29. Y. Mei *et al.*, Intrinsically disordered regions in autophagy proteins. *Proteins Struct., Funct. Bioinf.* **82**, 565–578 (2014).
30. A. Cristiani, A. Dutta, S. A. Poveda-Cuevas, A. Kern, R. M. Bhaskara, Identification of potential selective autophagy receptors from protein-content profiling of autophagosomes. *J. Cell. Biochem.* 1–14 (2023).
31. S. Naudi-Fabra, M. Tengo, M. R. Jensen, M. Blackledge, S. Milles, Quantitative description of intrinsically disordered proteins using single-molecule FRET, NMR, and SAXS. *J. Am. Chem. Soc.* **143**, 20109–20121 (2021).
32. G. Tesei *et al.*, Conformational ensembles of the human intrinsically disordered proteome. *Nature* **626**, 897–904 (2024).
33. J. M. Lotthammer, G. M. Ginell, D. Griffith, R. J. Emenecker, A. S. Holehouse, Direct prediction of intrinsically disordered protein conformational properties from sequences. *Nat. Methods* **21**, 1–12 (2024).
34. U. R. Shrestha, J. C. Smith, L. Petridis, Full structural ensembles of intrinsically disordered proteins from unbiased molecular dynamics simulations. *Commun. Biol.* **4**, 243 (2021).
35. R. Alessandri *et al.*, Pitfalls of the Martini model. *J. Chem. Theory Comput.* **15**, 5448–5460 (2019).
36. L. Monticelli *et al.*, The Martini coarse-grained force field: Extension to proteins. *J. Chem. Theory Comput.* **4**, 819–834 (2008).
37. S. J. Marrink, H. J. Risselada, S. Yefimov, D. P. Tieleman, A. H. De Vries, The Martini force field: Coarse-grained model for biomolecular simulations. *J. Phys. Chem. B.* **111**, 7812–7824 (2007).
38. A. H. Larsen *et al.*, Combining molecular dynamics simulations with small-angle X-ray and neutron scattering data to study multi-domain proteins in solution. *PLoS Comput. Biol.* **16**, e1007870 (2020).
39. J. Zavadlav, M. N. Melo, S. J. Marrink, M. Praprotnik, Adaptive resolution simulation of polarizable supramolecular coarse-grained water models. *J. Chem. Phys.* **142**, 244118 (2015).
40. L. Borges-Araújo, P. C. Souza, F. Fernandes, M. N. Melo, Improved parameterization of phosphatidylinositide lipid headgroups for the Martini 3 coarse-grain force field. *J. Chem. Theory Comput.* **18**, 357–373 (2021).
41. T. A. Wassenaar, H. I. Ingólfsson, R. A. Bockmann, D. P. Tieleman, S. J. Marrink, Computational lipidomics with insane: A versatile tool for generating custom membranes for molecular simulations. *J. Chem. Theory Comput.* **11**, 2144–2155 (2015).
42. F. E. Thomasen, F. Pesce, M. A. Roesgaard, G. Tesei, K. Lindorff-Larsen, Improving Martini 3 for disordered and multidomain proteins. *J. Chem. Theory Comput.* **18**, 2033–2041 (2022).

43. A. B. Poma, M. Cieplak, P. E. Theodorakis, Combining the Martini and structure-based coarse-grained approaches for the molecular dynamics studies of conformational transitions in proteins. *J. Chem. Theory Comput.* **13**, 1366–1374 (2017).
44. E. W. Martin *et al*., Interplay of folded domains and the disordered low-complexity domain in mediating hnRNPA1 phase separation. *Nucleic Acids Res.* **49**, 2931–2945 (2021).
45. F. Yu, S. Sukenik, Structural preferences shape the entropic force of disordered protein ensembles. *J. Phys. Chem. B* **127**, 4235–4244 (2023).
46. W. F. Zeno, W. T. Snead, A. S. Thatte, J. C. Stachowiak, Structured and intrinsically disordered domains within Amphiphysin1 work together to sense and drive membrane curvature. *Soft Matter* **15**, 8706–8717 (2019).
47. W. T. Snead, C. C. Hayden, J. C. Stachowiak, Membrane fission by protein crowding. *Biophys. J.* **110**, 574a (2016).
48. J. C. Stachowiak, C. C. Hayden, D. Y. Sasaki, Steric confinement of proteins on lipid membranes can drive curvature and tubulation. *Proc. Natl. Acad. Sci. U.S.A.* **107**, 7781–7786 (2010).
49. M. E. Oates *et al*., D^2P^2: Database of disordered protein predictions. *Nucleic Acids Res.* **41**, D508–D516 (2012).
50. S. F. Altschul *et al*., Gapped BLAST and PSI-BLAST: A new generation of protein database search programs. *Nucleic Acids Res.* **25**, 3389–3402 (1997).
51. J. Jumper *et al*., Highly accurate protein structure prediction with AlphaFold. *Nature* **596**, 583–589 (2021).
52. C. Kutzner *et al*., GROMACS in the cloud: A global supercomputer to speed up alchemical drug design. *J. Chem. Inf. Model.* **62**, 1691–1711 (2022).
53. J. Huang *et al*., CHARMM36m: An improved force field for folded and intrinsically disordered proteins. *Nat. Methods* **14**, 71–73 (2017).
54. U. Essmann *et al*., A smooth particle mesh Ewald method. *J. Chem. Phys.* **103**, 8577–8593 (1995).
55. B. Hess, H. Bekker, H. J. Berendsen, J. G. Fraaije, LINCS: A linear constraint solver for molecular simulations. *J. Comput. Chem.* **18**, 1463–1472 (1997).
56. S. Nosé, A molecular dynamics method for simulations in the canonical ensemble. *Mol. Phys.* **52**, 255–268 (1984).
57. S. Nosé, A unified formulation of the constant temperature molecular dynamics methods. *J. Chem. Phys.* **81**, 511–519 (1984).
58. W. G. Hoover, Canonical dynamics: Equilibrium phase-space distributions. *Phys. Rev. A* **31**, 1695 (1985).
59. M. Parrinello, A. Rahman, Polymorphic transitions in single crystals: A new molecular dynamics method. *J. Appl. Phys.* **52**, 7182–7190 (1981).
60. W. Kabsch, C. Sander, Dictionary of protein secondary structure: Pattern recognition of hydrogen-bonded and geometrical features. *Biopolym. Orig. Res. Biomol.* **22**, 2577–2637 (1983).
61. G. Bussi, D. Donadio, M. Parrinello, Canonical sampling through velocity rescaling. *J. Chem. Phys.* **126**, 014101 (2007).
62. H. J. Berendsen, J. V. Postma, W. F. Van Gunsteren, A. DiNola, J. R. Haak, Molecular dynamics with coupling to an external bath. *J. Chem. Phys.* **81**, 3684–3690 (1984).
63. J. D. Durrant, R. E. Amaro, Lipidwrapper: An algorithm for generating large-scale membrane models of arbitrary geometry. *PLoS Comput. Biol.* **10**, e1003720 (2014).
64. D. Boda, D. Henderson, The effects of deviations from Lorentz-Berthelot rules on the properties of a simple mixture. *Mol. Phys.* **106**, 2367–2370 (2008).
65. F. E. Thomasen *et al.*, Recalibration of protein interactions in Martini 3. bioRxiv [Preprint] (2023). https://doi.org/10.1101/2023.05.29.542689 (Accessed 20 August 2023).
66. T. A. Wassenaar, K. Pluhackova, R. A. Bockmann, S. J. Marrink, D. P. Tieleman, Going backward: A flexible geometric approach to reverse transformation from coarse grained to atomistic models. *J. Chem. Theory Comput.* **10**, 676–690 (2014).
67. P. J. Fleming, K. G. Fleming, HullRad: Fast calculations of folded and disordered protein and nucleic acid hydrodynamic properties. *Biophys. J.* **114**, 856–869 (2018).
68. N. Michaud-Agrawal, E. J. Denning, T. B. Woolf, O. Beckstein, MDAnalysis: A toolkit for the analysis of molecular dynamics simulations. *J. Comput. Chem.* **32**, 2319–2327 (2011).
69. D. R. Stirling *et al*., Cellprofiler 4: Improvements in speed, utility and usability. *BMC bioinform.* **22**, 1–11 (2021).
70. S. A. Poveda-Cuevas *et al.*, Data files for "Intrinsically disordered region amplifies membrane remodeling to augment selective ER-phagy". Zenodo. https://doi.org/10.5281/zenodo.13839066. Deposited 25 September 2024.